Using High-Resolution Simulations to Quantify Underestimates of Tornado Intensity from In Situ Observations

NATHAN A. DAHL AND DAVID S. NOLAN

Rosenstiel School of Marine and Atmospheric Science, University of Miami, Miami, Florida

GEORGE H. BRYAN AND RICHARD ROTUNNO

National Center for Atmospheric Research, Boulder, Colorado

(Manuscript received 7 September 2016, in final form 5 December 2016)

ABSTRACT

Large-eddy simulations are used to produce realistic, high-resolution depictions of near-surface winds in translating tornadoes. The translation speed, swirl ratio, and vertical forcing are varied to provide a range of vortex intensities and structural types. Observation experiments are then performed in which the tornadoes are passed over groups of simulated sensors. Some of the experiments use indestructible, error-free anemometers while others limit the range of observable wind speeds to mimic the characteristics of damage indicators specified in the enhanced Fujita (EF) scale. Also, in some of the experiments the sensors are randomly placed while in others they are positioned in regularly spaced columns perpendicular to the vortex tracks to mimic field project deployments.

Statistical analysis of the results provides quantitative insight into the limitations of tornado intensity estimates based on damage surveys or in situ measurements in rural or semirural areas. The mean negative bias relative to the "true" global maximum 3-s gust at 10 m AGL (the standard for EF ratings) exceeds 10 m s^{-1} in all cases and 45 m s^{-1} in some cases. A small number of sensors are generally sufficient to provide a good approximation of the running time-mean maximum during the period of observation, although the required spatial resolution of the sensor group is still substantially higher than that previously attained by any field program. Because of model limitations and simplifying assumptions, these results are regarded as a lower bound for tornado intensity underestimates in rural and semirural areas and provide a baseline for further inquiry.

1. Introduction

Measuring near-surface wind speeds in tornadoes is notoriously difficult. General-use, fixed-location instruments are ill suited to the task due to their lack of areal coverage, the relatively sporadic occurrence of tornadoes, and the hostile environment created by extreme winds and debris within the vortex. Thus, assessments of tornado intensity at specific locations are commonly forced to rely on damage as a proxy for wind speed, with wind–damage relationships obtained from engineering estimates and codified in systems such as the Fujita scale (Fujita 1971) and later the enhanced Fujita (EF) scale (Wind Science and Engineering Center 2006). However, it has been noted (e.g., Reynolds 1971; Doswell and Burgess 1988; Marshall 2002; Doswell et al. 2009; Edwards et al. 2013) that such wind speed inferences are rife with uncertainty. For instance, the prior integrity of heavily damaged structures is often difficult to determine, the effects of debris impacts may be conflated with damage inflicted by the winds alone, and the relative impact of wind duration versus intensity is poorly understood.

Advances in remote sensing technology have mitigated the problem of areal coverage and precipitated a dramatic increase in accumulated wind data from tornadoes. Mobile Doppler radars enable the collection of high-resolution swaths of measurements from the tornado and its immediate environment, which has greatly enhanced understanding of tornado morphology, intensity, and evolution for a growing number of events (e.g., Wurman and Gill 2000; Burgess et al. 2002; Kosiba et al. 2013; Houser et al. 2015; Wakimoto et al. 2015).

Corresponding author e-mail: Nathan A. Dahl, dahl_nathan@ou.edu

DOI: 10.1175/MWR-D-16-0346.1

However, tornadic wind radar data within 10 m of the ground (the standard level for EF scale wind estimates) are sparse and the relationship between radar-measured wind speeds at higher altitudes and actual wind speeds near the surface is unclear, with recent observations (Kosiba and Wurman 2013; Wurman et al. 2013) running counter to the common assumption that winds at typical in situ observation levels of 2–10 m AGL will be discernibly weaker than radar-measured winds aloft due to the influence of friction within the tornado boundary layer (e.g., stated in Wurman et al. 2007). Furthermore, Doppler radar estimates of tornado intensity carry substantial uncertainty due to factors such as spatial averaging within the resolution volume and differences between the motion of scatterers and the actual flow (e.g., due to centrifuging; Dowell et al. 2005; Snyder and Bluestein 2014).

In light of these uncertainties, direct observations of near-surface tornadic winds are highly desirable. Historically, in situ measurements of conditions within tornadoes [e.g., see Table 1 of Karstens et al. (2010)] have largely been limited to pressure fluctuations obtained through chance encounters with fixed instruments, although wind data have also been obtained in a few such cases (e.g., Fujita 1970; Blanchard 2013; Kato et al. 2015). Starting in the latter part of the twentieth century, increasing efforts have focused on developing specially designed portable probes and deploying them within tornadoes through a variety of means (e.g., Agee 1970; Colgate 1982; Bedard and Ramzy 1983; Bluestein 1983; Brock et al. 1987; Rasmussen et al. 1994; Samaras and Lee 2004; Wurman et al. 2007, 2012). Whether planned or unplanned, in situ pressure and wind transects of tornadoes have been obtained by mobile mesonets (Blair et al. 2008), instrument pods (Winn et al. 1999; Samaras and Lee 2004; Lee et al. 2004; Wurman and Samaras 2004; Lee et al. 2011), and vehicles specifically designed for tornado intercepts (Wurman et al. 2013).

However, the question remains as to how well those measurements correspond to the actual intensity of the tornadoes during the times of observation. Doswell and Burgess (1988) discuss causes for the bias toward heavily populated areas in damage-based tornado intensity assessments described by Schaefer and Galway (1982), and similar reasoning may be applied to tornado intensity assessments based on in situ observations. Put briefly, a sparse in situ network is more likely to miss the most intense part of the tornado and, hence, is more prone to producing a larger underestimate of the tornado's strength. This issue is highlighted when one considers the complexity of a tornadic wind field (particularly with respect to local enhancement from subvortices with diameters on the order of 10 m) and the scarcity of instruments in past field projects [e.g., single-instrument deployments in Samaras and Lee (2004) and Lee et al. (2004) or spacing on the order of 100 m or more in Rasmussen et al. (1994), Wurman et al. (2012), and Kato et al. (2015)]. Thus, even when probe observations inside tornadoes are obtained, they tend to be isolated, and cases in which multiple probes have intercepted a single tornado are exceptionally rare. Furthermore, most of those cases involve surface pressure measurements only; to our knowledge, the only instance of a single tornado impacting two anemometers occurred near Beloit, Kansas, on 29 May 2008, as documented in Karstens et al. (2010).

Obviously, without knowing the actual maximum wind speed, it is impossible to quantify this underestimate using the existing observational record. An alternative approach is to produce synthetic observations by placing simulated instruments within a realistic numerical simulation and compare "observed" maxima to the known state of the model. Uhlhorn and Nolan (2012) applied this method to hurricanes by generating aircraft wind observations from a simulation (Nolan et al. 2009a,b) of Hurricane Isabel (2003) and found a typical maximum 1-min wind speed underestimate of 7%–10%. Nolan et al. (2014) generated fixed anemometer observations from a hurricane "nature run" (Nolan et al. 2013) and found a typical underestimate of 10%–20%, even for optimal sampling. In this paper, we apply a similar approach to high-resolution tornado simulations in an effort to obtain quantitative insight into the expected underestimate of maximum wind speeds based on the availability of in situ tornado observations. Section 2 describes the numerical model framework for the simulations and the method used to obtain synthetic observations. Section 3 describes the wind output from the simulations. Section 4 analyzes the results from the observation experiments and provides statistical comparisons between the observations and the "true" intensity of the simulated vortices. Finally, section 5 discusses the implications and suggests topics for future study.

2. Experimental method

a. *Model framework*

To obtain realistic vortices to serve as the true state for our experiments, we use the "Fiedler chamber" approach (Fiedler 1994; Nolan 2005; Rotunno 2013) consisting of a closed chamber with a specified constant

rotation rate Ω. The fluid in the chamber is dry and isentropic. Instead of latent heating, the updraft is driven by a forcing function applied to the vertical velocity equation within an elliptical "bubble" fixed at the center axis. We follow Nolan (2005) by defining the forcing function, which varies by altitude z and horizontal distance r from the center axis, as

$$F_z(r,z) = \begin{cases} F_{\max}\cos\left(\frac{\pi}{2}\chi\right) & \text{for} \quad \chi < 1 \\ 0 & \text{for} \quad \chi \geq 1 \end{cases}, \tag{1}$$

where

$$\chi = \left[\frac{(z-z_b)^2}{l_z^2} + \frac{r^2}{l_r^2}\right]^{1/2}, \tag{2}$$

where z_b is the altitude of the center of the forcing bubble, and l_r and l_z are the horizontal and vertical radii of the forcing bubble, respectively. Here, we use $z_b = 8$ km, $l_r = 3$ km, and $l_z = 7$ km. In keeping with previous work (e.g., Fiedler and Garfield 2010), the model domain size is an order of magnitude greater than l_r to prevent the lateral boundaries from significantly affecting the results. Furthermore, as described in a companion paper (Rotunno et al. 2016), we apply Rayleigh damping in the upper part of the domain in order to prevent unrealistic reflection and recirculation of disturbances exiting the central updraft.

We use Cloud Model, version 1 (CM1; Bryan and Fritsch 2002), for these experiments. The formulation of this model is summarized in companion papers (Rotunno et al. 2016; Bryan et al. 2017a, hereafter BDNR; Nolan et al. 2017, hereafter NDBR), but a few pertinent details are repeated here for convenience. The fluid density is assumed to be constant. A compressible equation set is employed with a fixed sound speed of 300 m s^{-1}, which is integrated using the split-explicit method of Wicker and Skamarock (2002). The subgrid turbulence parameterization is described by BDNR. The domain extends 40 km horizontally and 15 km vertically. Based on the results of NDBR, a grid spacing of 5 m in the horizontal and 2.5 m in the vertical is deemed sufficient to resolve the crucial aspects of the near-surface vortex structure; this constant resolution is applied within a 4 km × 4 km box centered beneath the forcing function and extending upward from the surface to an altitude of 1 km. Outside the box, the grid stretches laterally and vertically to a maximum spacing of 220 m at the upper boundary and 248 m at the lateral boundaries. Free-slip boundary conditions are applied everywhere except the lower surface, which is semislip with a constant roughness length of 0.2 m.

b. Vortex simulation procedure

The size, intensity, and structure of simulated vortices are heavily influenced by the specified rotation rate and forcing function. To quantify the latter, we use a convective velocity scale based on (1) and (2):

$$W = \left[\int_{z_b-l_z}^{z_b+l_z} 2F_z(0,z)\,dz\right]^{1/2} = \sqrt{\frac{8F_{\max}l_z}{\pi}}. \tag{3}$$

To nondimensionalize the rotation rate, we use a swirl ratio:

$$S_r = \frac{\Omega l_r}{W}. \tag{4}$$

Based on the results of NDBR, we generally use W = 40 m s^{-1} (hereafter denoted W40) in order to produce wind speeds corresponding to the intensity range from EF0 to EF4, although an additional simulation with W = 60 m s^{-1} (W60) is used to obtain results for winds extending well into the EF5 range. Simulations are characterized as low swirl (S_r = 0.005, hereafter SR005), medium swirl (S_r = 0.01, SR01), and high swirl (S_r = 0.02, SR02).

Spinning up the three-dimensional simulations from rest is too costly due to the time required to obtain a mature, statistically steady vortex with fully developed resolved turbulence in the surface layer inflow. As described in BDNR, we reduce the cost of each simulation by proceeding in stages. We first integrate an inexpensive axisymmetric model with the same parameters to an approximate steady state, which provides the initial conditions for the full 3D simulation. Then, boundary layer eddies are generated in a smaller, three-dimensional, doubly periodic LES with the same rotation rate and surface roughness, using the technique of Bryan et al. (2017b). A time interval of 2000 s is used to spin up the eddies. Over a further 1800 s, velocity perturbations along a cross section from this simulation are written to a file and later "injected" at a distance r = 2 km from the center of the domain during the full 3D simulation, as explained by BDNR. Based on previous tests, we run the full 3D simulation for 1500 s to allow the vortex to adjust from the axisymmetric initial conditions and then record the instantaneous 10 m AGL wind speed (S10) every 0.1 s from t = 1500 to t = 1800 s.

This procedure is almost identical to the one used in NDBR. The simulations in that paper produced instantaneous S10 maxima reaching extreme values (exceeding 220 m s^{-1} in rare cases) but are generally confined to transient subvortices. The running 3-s

TABLE 1. List of simulations. Names and parameters for simulations in this study.

Simulation	Scale velocity ($m\,s^{-1}$)	Swirl ratio	Translation speed ($m\,s^{-1}$)
W40SR01U5	40	0.01	5
W40SR01U10	40	0.01	10
W40SR01U15	40	0.01	15
W40SR005U10	40	0.005	10
W40SR02U10	40	0.02	10
W60SR01U10	60	0.01	10

average of S10 at stationary locations (S10–3s) had maxima that were approximately 20% less than the instantaneous S10 maxima on average. We use a 3-s average to define a gust here, in keeping with current standards; the impact of varying the averaging period is illustrated later (section 3). Also, the global maximum value of S10–3s (i.e., the maximum occurring anywhere along the damage path) is the current standard used for rating tornadoes on the EF scale. However, considering the spatially and temporally sporadic nature of such maxima, NDBR argue that a time-averaged maximum S10–3s over a representative period would be a more fitting "damage potential" indicator. Therefore, both the global maximum S10–3s and the time-mean maximum S10–3s (calculated by obtaining the time series of the instantaneous maximum S10–3s and then averaging it over the time period corresponding to each swath) are considered here when evaluating observation errors.

The key difference between these simulations and those of NDBR is that here the lower boundary is translated westward relative to the model grid at 5, 10, or 15 $m\,s^{-1}$ (hereafter denoted U5, U10, and U15, respectively), yielding the variety of simulations listed in Table 1. The near-surface winds at locations in and around the vortex path from $t = 1500$ to $t = 1800$ s are postprocessed by positioning a 5-m resolution "truth" array measuring 0.7 km north–south and 1.5 km east–west with the west edge centered beneath the origin of the stored S10 array at $t = 1500$ s and shifting it westward at the same speed until $t = 1800$ s. Every 0.1 s, spline interpolation is used to map S10 from the model grid to the truth array. (Linear interpolation yields similar results but shows a greater tendency to smooth the peaks in the S10 fields.) The resulting time series are then used to generate swaths of maximum local instantaneous or time-averaged winds.

c. *Observation experiments procedure*

The issue of observational representativeness may be approached from a few different perspectives, each requiring its own experimental method. First, we examine a scenario in which a rural or semirural tornado randomly encounters standard damage indicators (DIs) used for EF damage ratings. The density of DIs in the ground survey for the 2013 El Reno tornado (Marshall et al. 2014) ranged from <1 to 26.7 km^{-2}, distributed by type as shown in Table 2. Using the El Reno case as a basis and motivated by the method used in Nolan et al. (2014) for hurricanes, we apply the following technique for sampling the wind swaths using independent "groups" of DIs:

- First, for each group, the number of DIs in the group is specified (n, hereafter referred to as the "group size").
- Then, a random location for each of the n DIs is selected within the region of the wind swath where strong winds

TABLE 2. EF scale damage indicator distribution. Description, maximum 10-m, 3-s gust, and 2013 El Reno tornado damage survey distribution of EF scale standard damage indicators (DIs). Data from Wind Science and Engineering Center (2006) and the Damage Assessment Toolkit survey database (courtesy of T. Marshall and G. Garfield).

DI	Description	Max S10–3s ($m\,s^{-1}$)	No. in El Reno survey
1	Small barns or farm outbuildings	58.5	90 (29.0%)
2	One- or two-family residences	88.5 (general) 98.3 (well constructed)	78 (25.2%)
3	Manufactured home—single wide	66.1	23 (7.4%)
4	Manufactured home—double wide	68.8	41 (13.2%)
9	Small professional building	89.4	2 (0.6%)
12	Large isolated retail building	89.8	7 (2.3%)
21	Metal building system	79.6	27 (8.7%)
22	Service station canopy	72.9	1 (0.3%)
24	Electrical transmission line	63.5 (wooden pole)	20 (6.5%
26	Free-standing poles	61.7	1 (0.3%)
27	Trees: Hardwood	74.6	20 (6.5%)

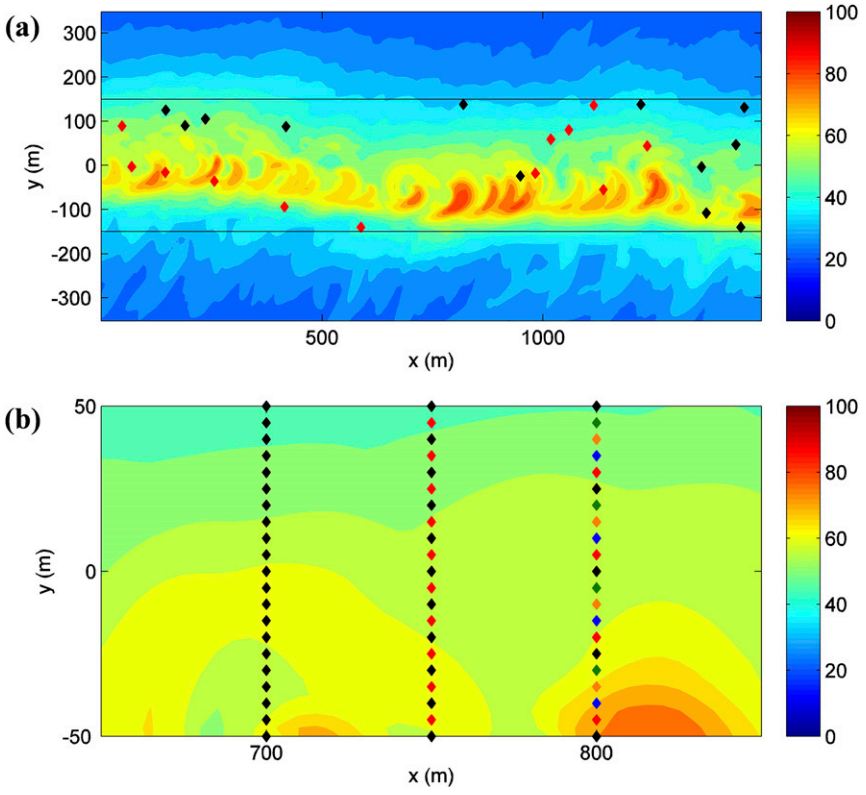

FIG. 1. (a) Two example random placements (one marked in black, the other in red) of a group of 12 sensors within the maximum 10-m, 3-s wind swath ($m\,s^{-1}$, shaded) for simulation W40SR01U10, generated as described in section 2. Black lines delineate the sampling region for random observation experiments. (b) Example placements for a column of anemometers at (left) 5-, (middle)10-, or (right) 25-m spacing within a zoomed portion of the swath described by the x and y axes. Different colors in a column denote different anemometer groups.

are likeliest, with the restriction that no location may contain more than one DI from the group (see Fig. 1a).
- Then, for each DI location, the maximum local S10–3s is determined, producing a ''sample'' of n measurements for the given group.
- The largest of the n measurements is then recorded as the group's maximum observed S10–3s, which is essentially the group's ''sample estimate'' of the global maximum S10–3s.
- The above procedure is repeated, with the DIs relocated at random between samples, to provide a ''set'' of 2000 sample estimates for each group size n for each swath.
- The mean and 5th and 95th percentiles of the sample estimates in each set are then calculated.

The DI locations are limited to the region within 150 m on either side of the track of the forcing function, in keeping with the average radius of maximum winds reported by Alexander and Wurman (2008); this region includes the location of the true global maximum S10–3s for all cases (see Fig. 2). Since this restriction yields a 0.45 km^2 sample region, the DI group size ranges from $n = 1$ to $n = 12$ to approximate the range of DI densities for the 2013 El Reno tornado. The type of DI that is placed at a given location is also selected at random from a probability distribution based on the relative frequencies of the DI types in the El Reno survey, shown in Table 2. (For example, each selected location has a 29.0% chance of being assigned DI 1, a 25.2% chance of being assigned DI 2, etc.)

We assume for these experiments (despite the sources of uncertainty noted in the introduction) that the local maximum S10–3s is perfectly related by the EF scale to the degree of damage (DOD) inflicted on each DI. Furthermore, we neglect the uncertainty associated with the range of wind speeds corresponding to each DOD. Essentially, the DIs are assumed to measure the local S10–3s perfectly unless it exceeds the maximum observable gust for the given DI type (i.e., the upper bound

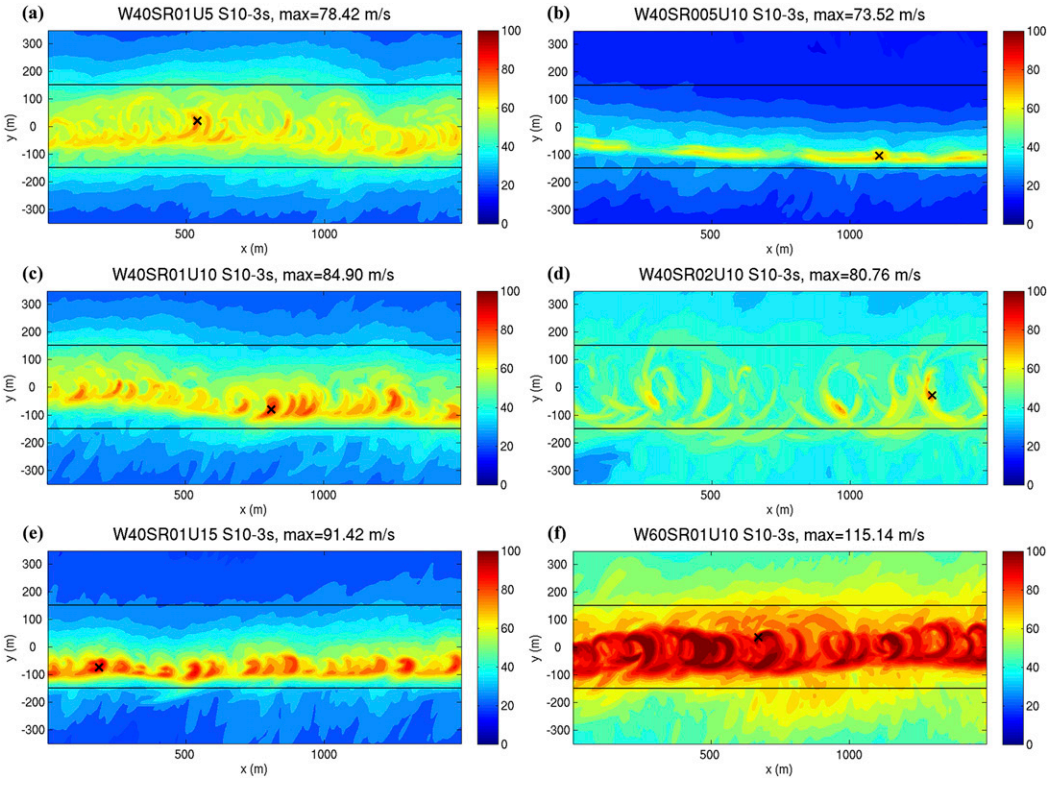

FIG. 2. Maximum 10-m, 3-s wind swaths ($m\,s^{-1}$) for simulations (a) W40SR01U5, (b) W40SR005U10, (c) W40SR01U10, (d) W40SR02U10, (e) W40SR02U15, and (f) W60SR01U10. Black "×" marks denote locations of global speed maxima. Black lines delineate sampling regions for random observation experiments.

for the maximum DOD), at which point the DI is assumed to be obliterated and the observed maximum local S10–3s is set to the corresponding value in Table 2.

A common source of uncertainty in damage surveys for intense tornadoes is the quality of construction for impacted one- or two-family residences (DI 2); a home that does not meet heightened construction standards, including the use of anchor bolts to attach the walls to the foundation, does not justify a maximum damage rating of EF5 if swept away (e.g., see Marshall 2002), and the fraction of residences that meet these standards is generally under 50% and varies widely by region (T. Marshall 2016, personal communication). To test the sensitivity of the results to this uncertainty, the experiments for simulation W60SR01U10 (the only case with S10–3s substantially greater than the "general" DI 2 upper limit in Table 2) are repeated with different fractions of general versus "well constructed" specified for instances of DI 2. (For example, since the chance of assigning a DI 2 at a given location is 25.2%, setting the well-constructed fraction to 50% means that a randomly selected location has a 12.6% chance of being assigned a general DI 2 and a 12.6% chance of being assigned a well-constructed DI 2.) Also, to quantify the underestimate due to the structural limitations of the DIs in each case, another set of sample estimates for each group size is obtained in which the DIs are replaced with indestructible anemometers that are assumed to provide error-free measurements of the local S10–3s ("perfect" anemometers).

We also wish to examine the limitations of measurements obtained from instruments deliberately placed in the tornado's path. Specifically, we deploy a regularly spaced group of perfect anemometers perpendicular to the vortex track as described in Rasmussen et al. (1994). We neglect the difference between wind measurements at 10 m AGL and the measurements at ≤1 m AGL typically obtained by field deployments, even though this difference may be quite large, because we wish to investigate a "best case" scenario with measurements corresponding exactly to the elevation used for the EF scale and because the model output below roughly 10 m AGL is heavily influenced by the turbulence parameterization as shown by BDNR.

As before, each sample provides the maximum S10–3s observed by a group of anemometers, this time from a north–south column spanning the wind swath. The anemometer spacing ranges from 5 m (n = 60) to 150 m

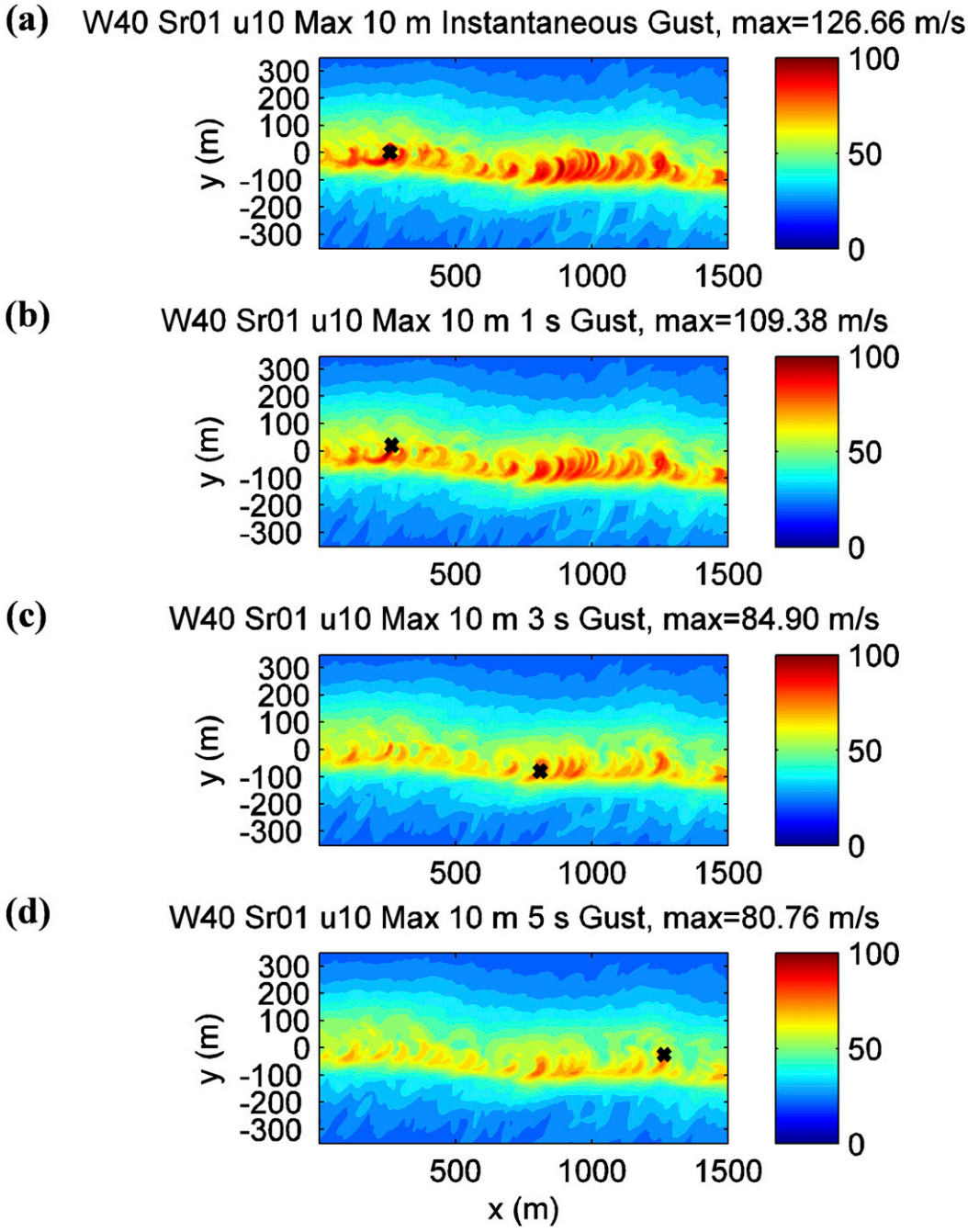

FIG. 3. Swaths of maximum 10-m (a) instantaneous, (b) 1-s average, (c) 3-s average, and (d) 5-s average wind speed ($m\,s^{-1}$) for simulation W40SR01U10.

($n = 2$). For 5-m spacing (which is the same as the numerical model grid spacing), one group of anemometers per swath column allows for a complete statistical analysis involving all grid points in the swath. For larger spacing, multiple separate groups of anemometers must be placed within each swath column to achieve the same purpose. As shown in Fig. 1b, this is done by placing each successive anemometer group one grid point (5 m) north of the previous group and repeating until all of the grid points in the column have been covered (e.g., 30 groups of anemometers per column for 150-m anemometer spacing), with a separate value of maximum observed S10–3s recorded for each group. Since there are 300 columns in each swath, this

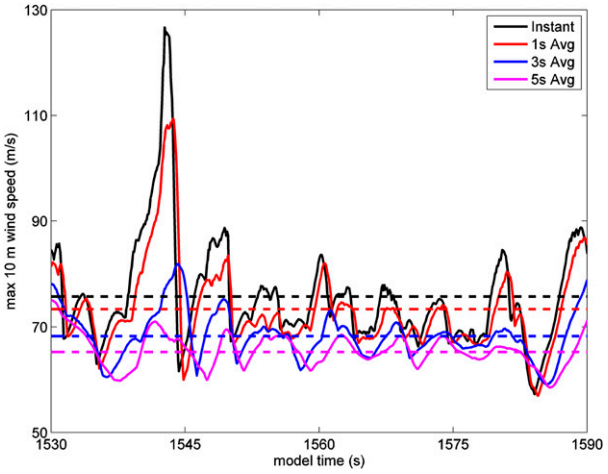

FIG. 4. Time series of global maximum 10-m instantaneous (black), 1-s (red), 3-s (blue), and 5-s (fuchsia) wind speed from $t = 1530$ to $t = 1590$ s for simulation W40SR01U10. Dashed lines indicate time means.

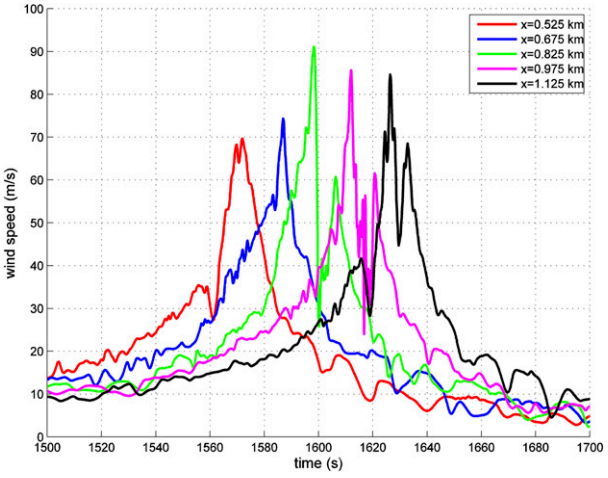

FIG. 5. Local time series of instantaneous 10-m wind speed from $t = 1500$ to $t = 1700$ s at maximum 10-m, 3-s gust locations along grid columns located at $x = 0.525$ km (red), 0.675 km (blue), 0.825 km (green), 0.975 km (fuchsia), and 1.125 km (black) for simulation W40SR01U10.

procedure yields a total number of samples ranging from 300 for 5-m anemometer spacing to 9000 for 150-m anemometer spacing. The results from each set of samples are then used to calculate the mean and 5th and 95th percentiles for the maximum observed wind speed for each spacing.

3. Simulated tornadic winds

a. *Wind swaths*

Figure 2 shows the swaths of local maximum S10–3s for all simulations. First, it is clear from Figs. 2a, 2c, and 2e that translation increases the maximum wind speed. This increase is not only due to the addition of rotational and translational velocity on the right side of the tornado, since a translation speed increase of $5\,m\,s^{-1}$ increases the maximum S10–3s by approximately $6.5\,m\,s^{-1}$ in this case. Rather, faster translation also elicits a shift toward a lower-swirl configuration (i.e., a narrower, more intense main vortex with stronger subvortices that are spatially less frequent and more confined to the right side). [This result agrees with the finding of Lewellen et al. (2000) that vortex translation has the effect of lowering the corner flow swirl ratio.]

As in NDBR, Fig. 2b shows that SR005 gives a consistent one-celled vortex with maximum S10 at a radius of approximately 25 m. However, the SR005 vortex in NDBR is very near the optimal "drowned vortex jump" configuration (see Fig. 6 in NDBR's paper) and has the most intense surface winds, whereas here it is the weakest of the simulations because the translation produces a lower-swirl vortex structure with a weaker, more elevated wind maximum. Figure 2d shows a two-celled vortex with the most intense subvortices at a radius of approximately 100 m for SR02, similar to NDBR. Interestingly, whereas the maximum winds are conventionally expected in the right-front quadrant of the vortex, here the maxima, associated with subvortices reaching peak intensity, are generally to the right-rear. Moreover, Fig. 2f shows several maxima, including the global maximum, to the left of the vortex center for simulation W60SR01U10.

As explained in section 2c, a 3-s averaging period is used for these results to conform to the standards used for the EF scale. The issue of time averaging merits some discussion here: since structures do not respond instantaneously to wind fluctuations, it seems reasonable to expect that the instantaneous wind speed maximum within the vortex will not be as representative of damage potential as the maximum gust averaged over some interval. For example, Phan and Simiu (1998) conclude that lengthy exposure to tornadic winds increased the damage produced by the 27 May 1997 Jarrell, Texas, tornado; similarly, Wurman et al. (2014) claim that the brevity of wind speed maxima at stationary points due to fast translation of subvortices within the 31 May 2013 tornado near El Reno, Oklahoma, may have contributed to lighter damage than would have been expected from the instantaneous radar measurements. However, the duration of the "most representative" averaging period is unclear; the specification of a 3-s gust is based on the observation interval of standard anemometers rather than the gust duration required to produce discernible

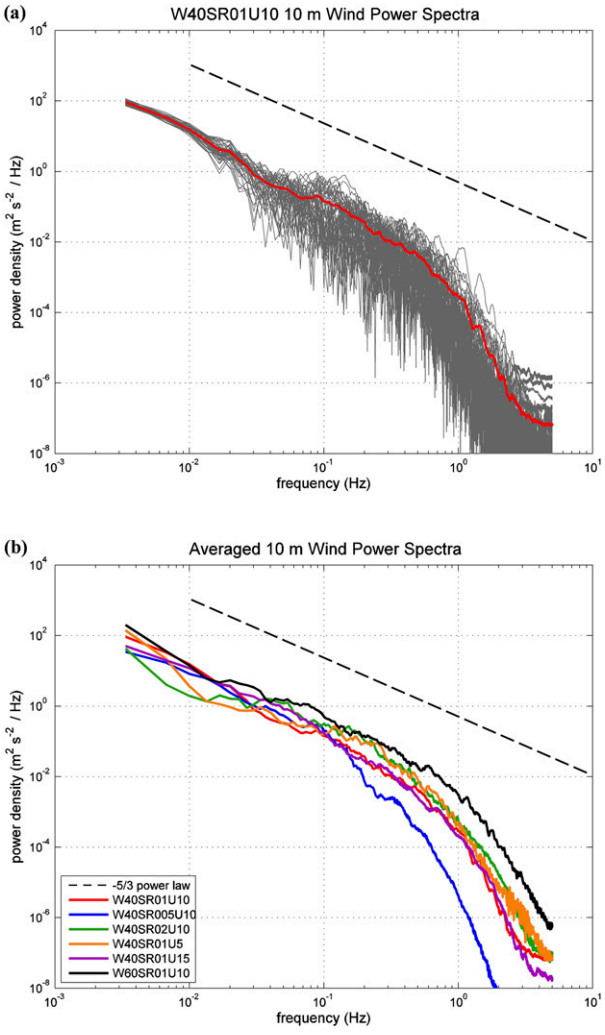

FIG. 6. (a) The 10-m wind power spectra from individual locations (gray) along the track of maximum 3-s gusts, along with the group average (red) for simulation W40SR01U10. (b) Average 10-m wind power spectra for simulations W40SR01U10 (red), W40SR005U10 (blue), W40SR02U10 (green), W40SR01U5 (orange), W40SR01U15 (purple), and W60SR01U10 (black). Dashed lines represent the −5/3 power law.

damage to a given structure (J. Schroeder 2016, personal communication).

Figures 3 and 4 illustrate the impact of time averaging on the wind swaths examined in this study. Time averaging, even over a 5-s period, does not have a large impact on the representation of the size and structure of the vortex; however, it reduces the time-mean global maximum S10 by approximately 10 m s^{-1} and the instantaneous global maximum by as much as 50 m s^{-1} for more intense subvortices, with the largest reduction generally seen when switching from a 1-s average to a 3-s average. Furthermore, the location of the maximum gust varies widely depending on which averaging period is used. Thus, the issue of which averaging period is most correlated with damage has significant implications when seeking to characterize tornado structure and intensity from surveys, although that topic is beyond our present scope.

b. *Power spectra*

To illustrate turbulence characteristics for the intense part of the tornado, power spectra were calculated from instantaneous S10 time series at locations of maximum winds along longitudinal slices. Example time series from W40SR01U10 are shown in Fig. 5; similar to the local observations in Blair et al. (2008) and Kato et al. (2015), an asymmetry is evident in the outer vortex, which is consistently stronger ahead of the core and weaker behind. Interestingly, the observations in Blanchard (2013) show the opposite, with wind speeds increasing rapidly from a smaller ''background'' value in advance of the tornado and decreasing gradually to a higher background value behind, although this may be due to differences in observation locations relative to surrounding asymmetric features such as rear-flank downdrafts (J. Marquis 2016, personal communication).

To ensure complete passage of the vortex and to mitigate the amount of detrending required for each time series, the samples were confined to the central half of the swath (i.e., from $x = 0.375$ to $x = 1.125$ km) for each case. Spectra of horizontal wind speed were calculated separately for 50 samples taken at 15-m intervals within this range and then averaged together. The separate and averaged results for W40SR01U10 are shown in Fig. 6a and the averaged results from all simulations are compared in Fig. 6b. Considering the proximity to the lower boundary and the rapid, intense, localized transitions in the wind field as the vortex translates, it is somewhat surprising to note the degree of agreement between the results and the energy spectrum predicted by the local isotropy theory of Kolmogorov (1941). With the exception of simulation W40SR005U10, the spectra generally follow a −5/3 slope for frequencies up to 1 Hz. It should be noted that we also calculated spectra intended to focus on winds within the tornado itself [i.e., S10–3s > 30 m s^{-1}, after Marshall et al. (2014)], with the time interval reduced in an effort to improve agreement with the stationarity assumption. However, the results were qualitatively similar to those in Fig. 6 and are therefore not shown here.

Departures from the Kolmogorov profile due to the effects of rotation on turbulent energy cascade have been noted in previous modeling experiments (e.g., Mininni and Pouquet 2010; Baerenzung et al. 2011), and we similarly note a subtle ''bottleneck'' between 0.1 and 1 Hz (more pronounced at higher swirl) corresponding

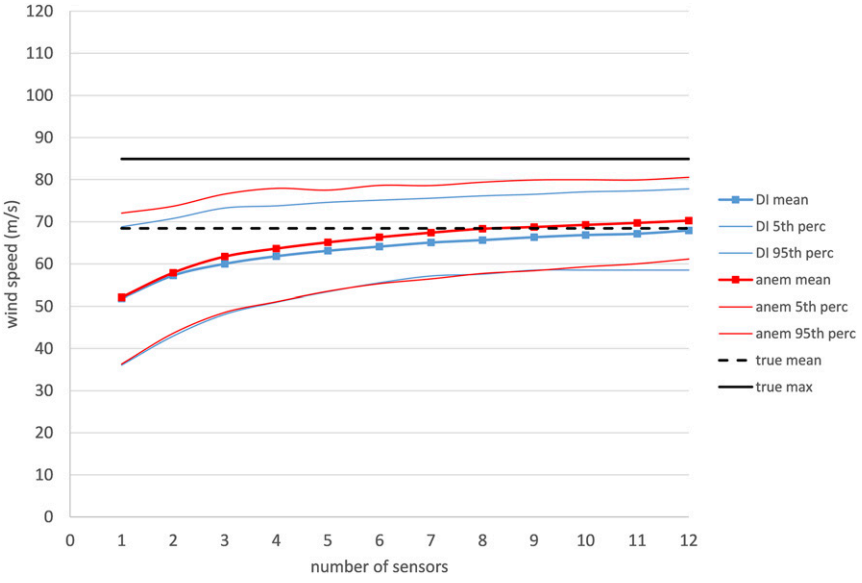

FIG. 7. Mean, 5th percentile, and 95th percentile of sample estimates of the global maximum 10-m, 3-s wind speed ($m\,s^{-1}$) plotted as a function of sensor group size from random placement damage indicator ("DI", blue) and perfect anemometer ("anem", red) experiments for simulation W40SR01U10, along with the true global maximum ("true max", solid black) and true time-mean maximum ("true mean," dashed black).

to cyclical development of subvortices and consequent wobbling of the main vortex. Above 1 Hz, the spectra drop off more steeply, which is attributable to limitations in model resolution; using Taylor's (1938) "frozen turbulence" hypothesis as a rough approximation and assuming a mean background wind speed of $30\,m\,s^{-1}$, a frequency >1 Hz indicates a mean eddy size <30 m, which is poorly resolved on the 5-m computational grid. This result agrees with the specification in Bryan et al. (2017b). that the cutoff frequency f_c in CM1 is related to the grid resolution Δ and the background wind speed U by

$$f_c \approx \frac{U}{6\Delta}. \tag{5}$$

This rule yields $f_c = 1$ Hz for $U = 30\,m\,s^{-1}$ and $\Delta = 5$ m. Furthermore, W40SR005U10, which has weaker winds in general (see Fig. 2), has a much lower cutoff frequency (essentially corresponding to the spatial scale of the main vortex in that case) whereas W60SR01U10, which has stronger winds, has a noticeably higher cutoff frequency.

4. Observation experiment results

a. Random damage indicators/anemometers

Figure 7 plots the mean sample estimate of the global maximum S10–3s (thick line) and the 5th and 95 percentiles (thin lines) for the DI experiments (blue) and the anemometer experiments (red) for W40SR01U10 as functions of group size n, along with the true global maximum (solid black line) and the true time-mean maximum (dashed black line). In this case, the mean underestimate of the global maximum S10–3s for a group of DIs ranges from $33\,m\,s^{-1}$ (39%) for $n = 1$ to $17\,m\,s^{-1}$ (20%) for $n = 12$, which is approximately double the mean relative underestimate reported by Nolan et al. (2014) for hurricanes. Furthermore, whereas only one or two sensors were required in that study to provide a good estimate (on average) of the time-mean maximum winds, here $n \geq 4$ is required to reduce the underestimate of the time-mean maximum to ≤10%. It is clear that spatial undersampling is the dominant source of error in this case, since replacing the DIs with anemometers produces only a slight improvement. Also, it should be noted that these results are not normally distributed; in this case, there is slight positive skewness in the distributions for both the DI experiments and the anemometer experiments.

Corresponding results for W40SR01U5 and W40SR01U15 are shown in Fig. 8. There is a clear relationship between the forward speed of the vortex and the quality of the observations. With a $5\,m\,s^{-1}$ translation speed, the mean underestimate of the true global maximum varies from $24\,m\,s^{-1}$ (29%) for $n = 1$ to $13\,m\,s^{-1}$ (17%) for $n = 12$, and the mean underestimate of the true time-mean maximum is below 10% for $n \geq 2$.

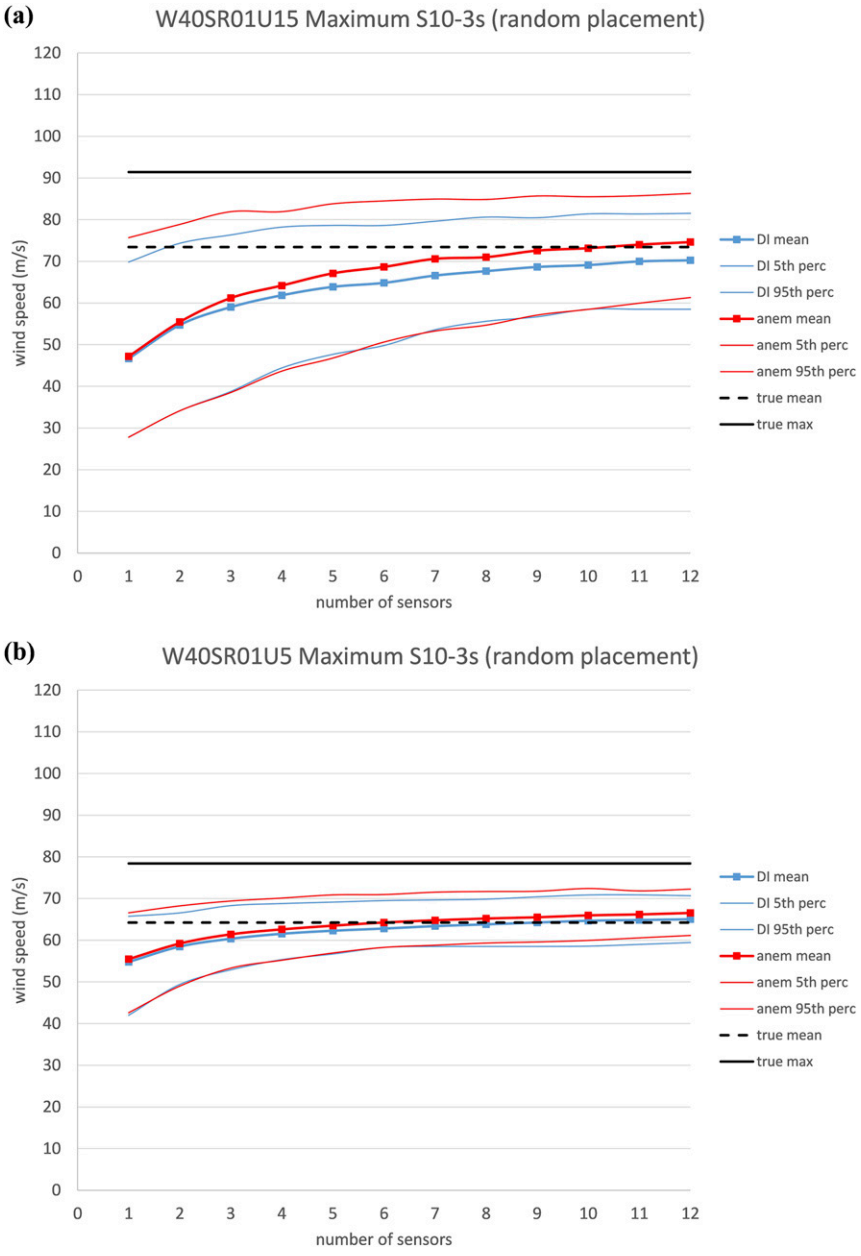

FIG. 8. As in Fig. 7, but for simulations (a) W40SR01U15 (narrower vortex) and (b) W40SR01U5 (broader vortex).

(Note that an increase in translation speed of $5\,\mathrm{m\,s^{-1}}$ corresponds to a $\sim 5\,\mathrm{m\,s^{-1}}$ increase in time-mean maximum S10–3s, both when comparing W40SR01U5 to W40SR01U10 and when comparing W40SR01U10 to W40SR01U15.) Furthermore, the range from the 5th percentile to the 95th percentile is greatly reduced. With a $15\,\mathrm{m\,s^{-1}}$ translation speed, the mean underestimate of the global maximum increases to $45\,\mathrm{m\,s^{-1}}$ (49%) for $n = 1$ and $21\,\mathrm{m\,s^{-1}}$ (23%) for $n = 12$, the mean underestimate of the time-mean maximum is only below 10% for $n \geq 7$, and the range from the 5th percentile to the 95th percentile is greatly increased. Furthermore, positive skewness is evident in the distribution at $n = 1$ for W40SR01U15. These changes are attributed to the structural differences between the wind swaths as illustrated in Fig. 2; as discussed previously, with the background swirl unchanged, the slower-moving tornado is noticeably broader and has weaker subvortices that revolve completely around the core while the faster-moving tornado is narrower (which exacerbates the

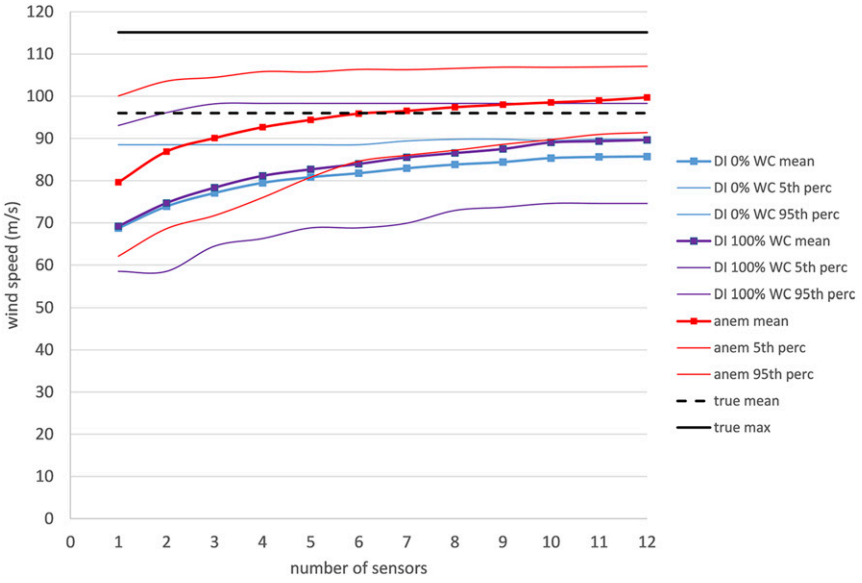

FIG. 9. As in Fig. 7, but for simulation W60SR01U10 and including results from damage indicator experiments with 0% ("0% WC", blue) and 100% ("100% WC", purple) of one- and two-family residences specified as "well constructed."

undersampling for small n) and has stronger subvortices that are generally confined to the right side.

Predictably, increasing the maximum winds also increases the impact of DI structural limitations; the DI results and the anemometer results are nearly identical for W40SR01U5, while the use of anemometers instead of DIs improves the mean estimate by approximately $5\,m\,s^{-1}$ at $n = 12$ for W40SR01U15. This finding is confirmed by the results for W60SR01U10 in Fig. 9, which show that the use of DIs instead of anemometers consistently increases the mean underestimate of the global maximum by $\geq 10\,m\,s^{-1}$. Furthermore, while the anemometer mean underestimate of the time-mean maximum falls below 10% by $n = 2$ and is nearly zero at $n = 5$, the DI mean underestimate does not fall below 10% until $n = 8$ when all instances of DI 2 are rated as well constructed ("100% WC," purple lines in the plot) and remains above 10% even at $n = 12$ when all instances of DI 2 are rated as general ("0% WC," blue lines in the plot).

Uncertainty in the construction of one- and two-family residences has a relatively minor impact on the mean, constituting a difference of $4\,m\,s^{-1}$ between 0% WC and 100% WC. However, the 95th percentile is substantially increased when the fraction of well-constructed residences is increased, and the combined effect markedly increases the probability of detecting winds over the EF5 threshold of $89.4\,m\,s^{-1}$, as shown in Table 3. Also, the limitations of the DIs artificially skew the results by truncating the upper part of the distribution, which is much more noticeable for 0% WC in Fig. 10. Of course, these findings are heavily influenced by the distribution of DIs in Table 2, since the vast majority of the nonresidential structures in that distribution have limits well below the EF5 threshold; however, in the absence of comprehensive data, it may be argued that the dependence of EF5 detection probability on the fraction of well-constructed residences could be even higher in more populated areas where "rural" structures (e.g., barns and outbuildings) are less prevalent.

To compare cases with lower and higher background swirl, the results from simulations W40SR005U10 and

TABLE 3. Probability of detecting EF5 winds for simulation W60SR01U10. Probability (%) of detecting winds above the EF5 threshold in simulation W60SR01U10 for different sensor group sizes and types. ("% WC" denotes the percentage of one- and two-family residences that are considered "well constructed" in each set of damage indicator samples.)

Group size n	0% WC	50% WC	100% WC	Anemometers
1	0.9	4.7	8.4	28.4
2	1.2	7.5	14.2	49.0
3	2.5	12.0	22.3	61.8
4	3.5	17.1	29.6	71.9
5	3.8	18.9	31.6	79.4
6	4.0	21.7	36.7	86.6
7	5.6	25.7	42.8	89.1
8	6.7	29.6	46.3	91.7
9	7.1	32.7	51.1	93.7
10	7.4	36.2	58.7	95.5
11	9.0	39.2	59.8	97.3
12	9.3	39.9	61.2	98.2

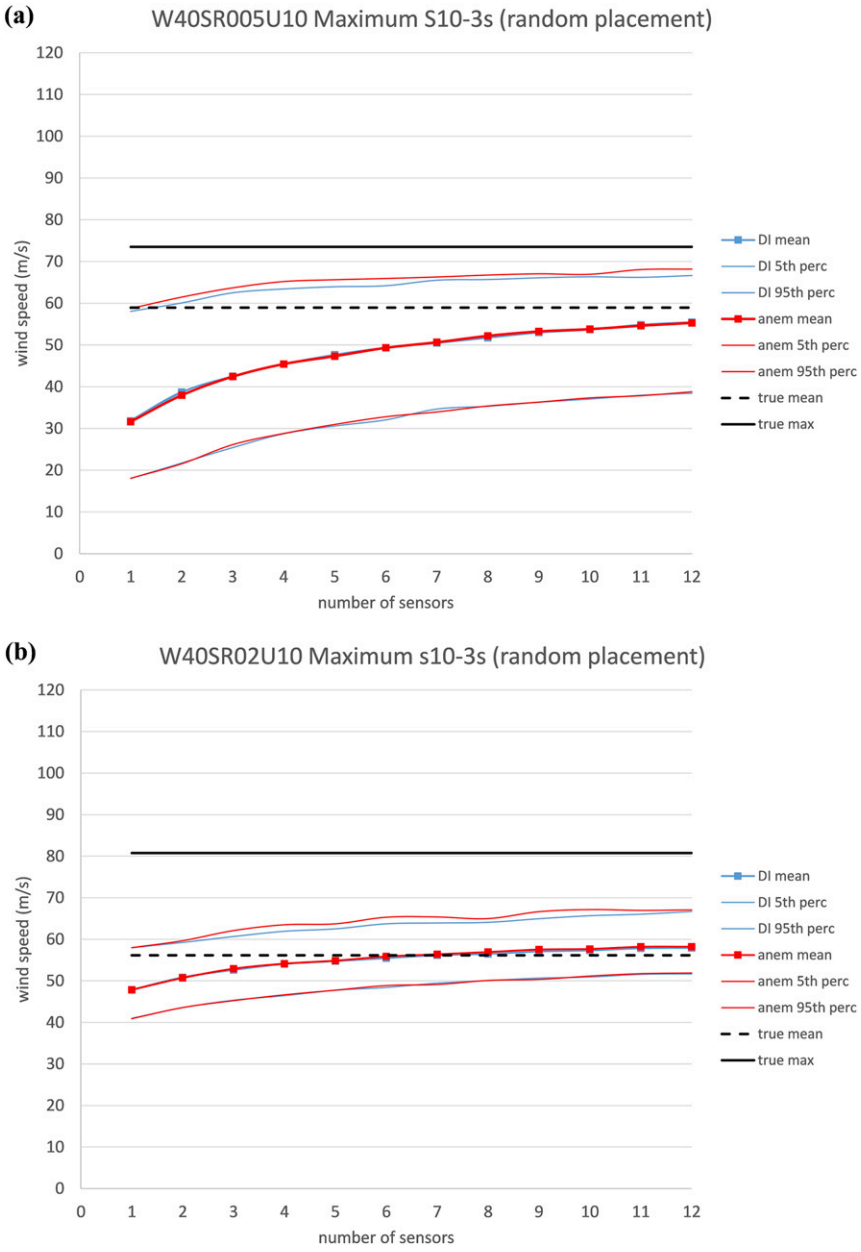

FIG. 10. As in Fig. 7, but for simulations (a) W40SR005U10 (narrower vortex) and (b) W40SR02U10 (broader vortex).

W40SR02U10 are shown in Fig. 10. As in the evaluation of W40SR01U5 and W40SR01U15, a narrower vortex is compared here to a broader vortex with more prominent subvortices. The sample estimate at large n of the global maximum is better for the narrower vortex in this instance (W40SR005U10); the opposite is true when comparing W40SR01U5 and W40SR01U15, in which case the narrower vortex (W40SR01U15) has the larger underestimate. However, there are some qualitative similarities as well; for instance, the distribution at small n is noticeably more skewed for the narrower vortex in both cases. Also, the range from the 5th percentile to the 95th percentile is much less for the broader vortex and there is less benefit from increasing the number of sensors than there is for the narrower vortex, with the mean underestimate of the global maximum reduced by $10\,\mathrm{m\,s^{-1}}$ from $n = 1$ to $n = 12$ for W40SR02U10 compared to a reduction of $24\,\mathrm{m\,s^{-1}}$ for W40SR005U10. Finally, a good estimate (<10% mean relative error) of the time-mean maximum is obtained

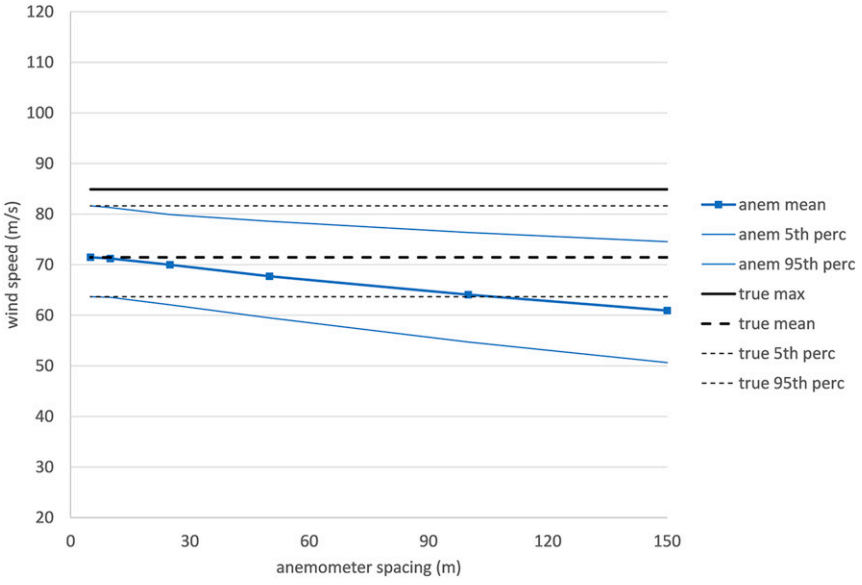

FIG. 11. Mean, 5th percentile, and 95th percentile of observed maximum 10-m, 3-s winds ($m\,s^{-1}$) from anemometer column experiments (''anem'') plotted as a function of anemometer spacing for simulation W40SR01U10, along with the true global maximum (''true max,'' thick solid black) and the along-track mean (''true mean,'' thick dashed black), 5th percentile (''true 5th perc,'' thin dashed black), and 95th percentile (''true 95th perc,'' thin dashed black) for the true columnar maximum.

more easily for the broader vortex (requiring $n \geq 2$ for W40SR02U10) than it is for the narrower vortex (requiring $n \geq 10$ for W40SR005U10), and DI structural limitations have a negligible impact in both cases.

b. Columns of anemometers

The mean (thick blue lines) and the 5th and 95th percentiles (thin blue lines) for the maximum S10–3s observed by a column of anemometers aligned perpendicular to the vortex track are plotted as functions of anemometer spacing in Figs. 11 through 16. In addition to determining how well the observations correspond to the true global maximum S10–3s (thick solid black lines), we also wish to determine how well these measurements correspond to the true maximum intensity along the column being sampled by the anemometers. (In terms of field deployments, this procedure is akin to placing a series of anemometers on a road and attempting to measure the maximum wind speed occurring anywhere along that road as the tornado passes.) Thus, the true maximum S10–3s along each column of grid points for each case is also recorded and means (thick dashed black lines) and 5th and 95th percentiles (thin dashed black lines) are calculated from the results to provide a true mean ''columnar'' maximum and an indication of the along-path variation in tornado intensity. Note that the mean columnar maximum is not the same as the time-mean maximum used for the random placement experiments, which follow the method of Nolan et al. (2014), although the difference is quite small for these simulations.

Comparing the true global maximum and the true mean columnar maximum approximates the expected underestimate due purely to fluctuations in intensity as the vortex translates, even if a perfect anemometer is placed ideally to observe the maximum S10–3s along a given column. For example, the difference between ''true mean'' and ''true max'' in Fig. 12 gives an expected error of $13\,m\,s^{-1}$ due to intensity fluctuations for W40SR01U15. Also, to evaluate how well the observations reflect actual fluctuations in intensity, correlation coefficients between true and observed columnar maxima are calculated for each swath for anemometer spacings ≥ 10 m (obviously, the correlation for 5 m spacing is 1) as follows:

$$r = \frac{\sum_{i=1}^{k}[(T_i - \overline{T})(O_i - \overline{O})]}{\sqrt{\left[\sum_{i=1}^{k}(T_i - \overline{T})^2\right]\left[\sum_{i=1}^{k}(O_i - \overline{O})^2\right]}}, \tag{6}$$

where T_i and O_i are the true and observed maxima for the i th column, respectively; k (=300) is the number of

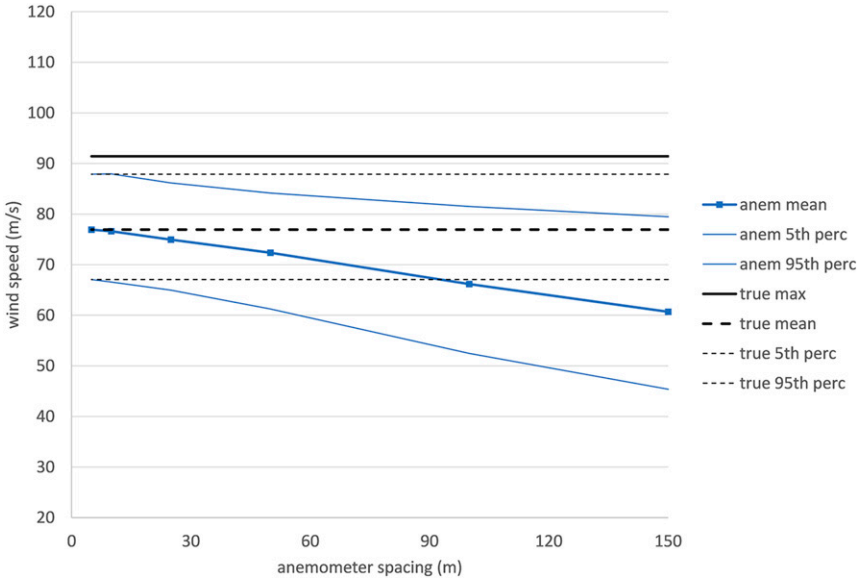

FIG. 12. As in Fig. 11, but for simulation W40SR01U15.

columns in each swath; and an overbar denotes averaging over k. The results are listed in Table 4.

The expected error due to intensity fluctuations varies from case to case, with a maximum value of 22 m s^{-1} for W40SR02U10 (see Fig. 16). As might be expected, this error is most closely tied to background swirl and larger errors tend to be associated with maxima confined to transient, widely spaced subvortices (see Fig. 2). The remaining error is due to spatial undersampling and seems to vary almost linearly with anemometer spacing. At 150-m spacing, it ranges from 7 m s^{-1} for W40SR01U5 (see Fig. 13) and 10 m s^{-1} for W60SR01U10 (see Fig. 14) to 20 m s^{-1} for W40SR005U10 (see Fig. 15). In general, it appears that the spacing must be sufficiently small to obtain three or more simultaneous anemometer measurements within the vortex in order to reduce the mean spatial undersampling error to <10%. For instance, using the trend in Fig. 15 suggests that ~ 40-m spacing would be required for this purpose in the case of W40SR005U10 (which appears from Fig. 2 to have a diameter of approximately 100–150 m based on the region of wind speeds >30 m s^{-1}), while doing the same with Fig. 16 suggests that ~ 140-m spacing would be sufficient for the case of W40SR02U10 (which has a diameter of approximately 400–450 m).

According to the data in Table 4, an even more stringent resolution requirement may be warranted. In all cases, correlation between the true and observed columnar maxima begins to decline sharply with increased spacing between 25 and 50 m. This decline is somewhat lessened for W40SR01U10, W40SR01U15, and W40SR02U10, but there is no obvious pattern in terms of vortex size, structure, or maximum wind speed to explain these differences. For now, we simply note that the minimum number of vortex transects suggested by these results for an accurate, reliable description of the most intense part of a tornado is beyond the attainments of any previous field campaign.

5. Summary and conclusions

This study uses observation experiments performed on high-resolution simulations of translating tornadoes to provide quantitative insight regarding the uncertainty

TABLE 4. "Observed"/"true" columnar S10–3s maxima correlation. Correlation r between maximum S10–3s observed by a column of perfect anemometers and the "true" column maximum S10–3s from simulated wind swaths.

Anemometer spacing (m)	W40SR01U10	W40SR01U5	W40SR01U15	W40SR005U10	W40SR02U10	W60SR01U10
10	0.9974	0.9915	0.9964	0.9948	0.9955	0.9918
25	0.9514	0.8763	0.9276	0.8913	0.9455	0.9084
50	0.7970	0.6751	0.7995	0.6567	0.8170	0.7359
100	0.5679	0.4662	0.4401	0.2714	0.5925	0.5531
150	0.4167	0.3451	0.2536	0.1658	0.4544	0.4628

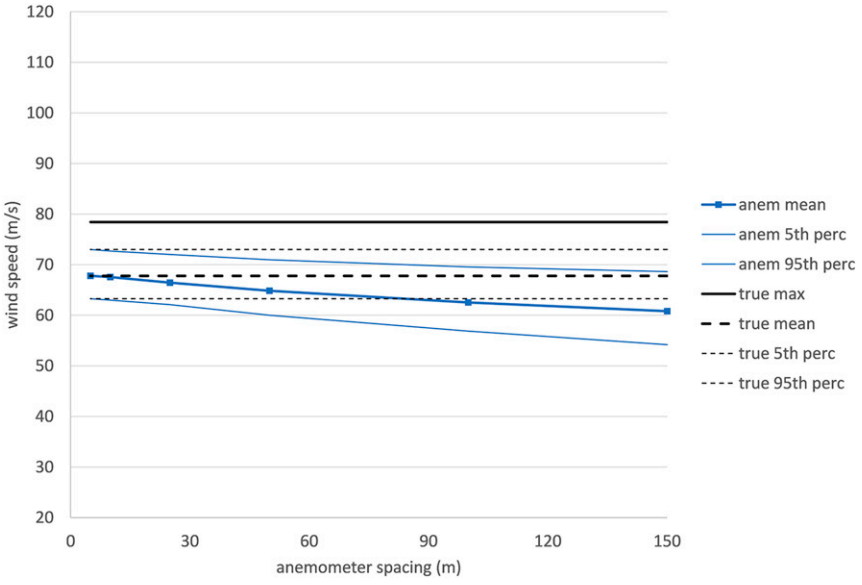

FIG. 13. As in Fig. 11, but for simulation W40SR01U5.

of maximum wind speed estimates from damage surveys in rural or semirural locations as well as deliberate or "chance" encounters with in situ instruments. The spatial density and categorical distribution of damage indicators (DIs) from the 31 May 2013 tornado near El Reno, Oklahoma, were used as a basis for randomly placing groups of DIs in the wind swaths generated from the simulations. For each case, we consider both the "global" maximum 10-m, 3-s wind speed (S10–3s) occurring anywhere in the swath and the "time-mean" maximum S10–3s obtained by finding the maximum S10–3s at each model output time over the period corresponding to the swath and then averaging the resulting time series.

When using randomly placed groups of perfect anemometers to estimate the maximum S10–3s from a large number of samples, we find that mean underestimates of the true global maximum S10–3s (the hypothetical basis for an EF scale rating) due to spatial undersampling exceed $10\,\mathrm{m\,s^{-1}}$ in all cases and approach $45\,\mathrm{m\,s^{-1}}$ in

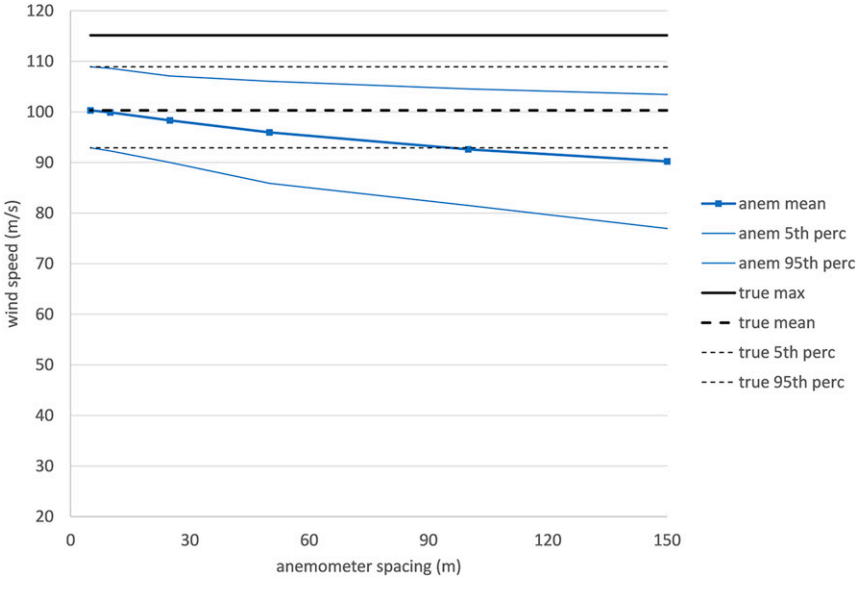

FIG. 14. As in Fig. 11, but for simulation W60SR01U10.

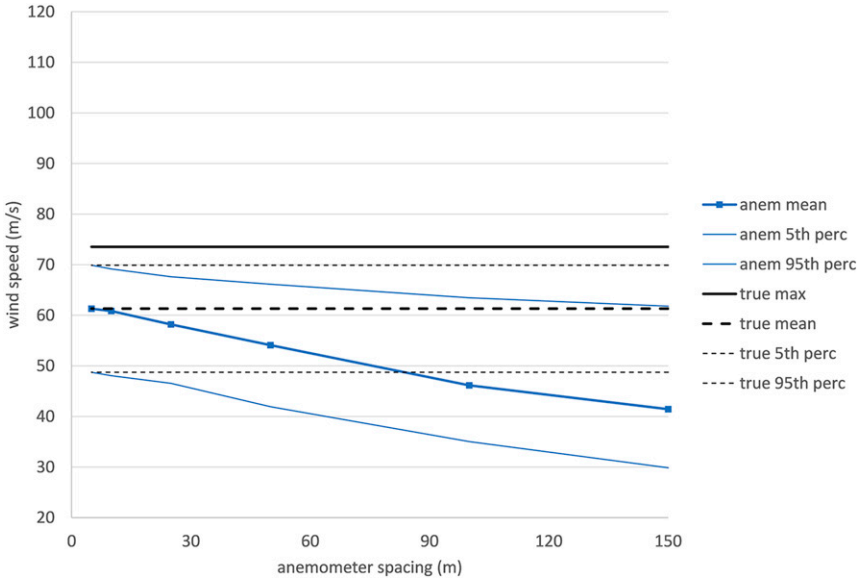

FIG. 15. As in Fig. 11, but for simulation W40SR005U10.

some cases when DIs or anemometers are particularly sparse. In general, a semirural DI or anemometer distribution appears to be sufficient to provide a good estimate of the time-mean maximum S10–3s in all but the most violent cases. We also find that good estimates of the time-mean maximum S10–3s are noticeably easier to obtain for broader vortices.

We also find that the structural limitations of the DIs only contribute substantially to measurement error (on average) for tornadoes with maximum S10–3s above the EF5 threshold. However, in that event, the likelihood of failing to detect EF5 winds through a survey of DIs is high in rural areas regardless of residential construction quality, even for a tornado that is clearly and consistently above the EF5 threshold. Moreover, the likelihood remains above 50% in semirural areas under the ''best current'' scenario for construction quality (i.e., with half of the residences qualifying as ''well constructed''). Even under optimal conditions in which all residences are well constructed, the probability of failing

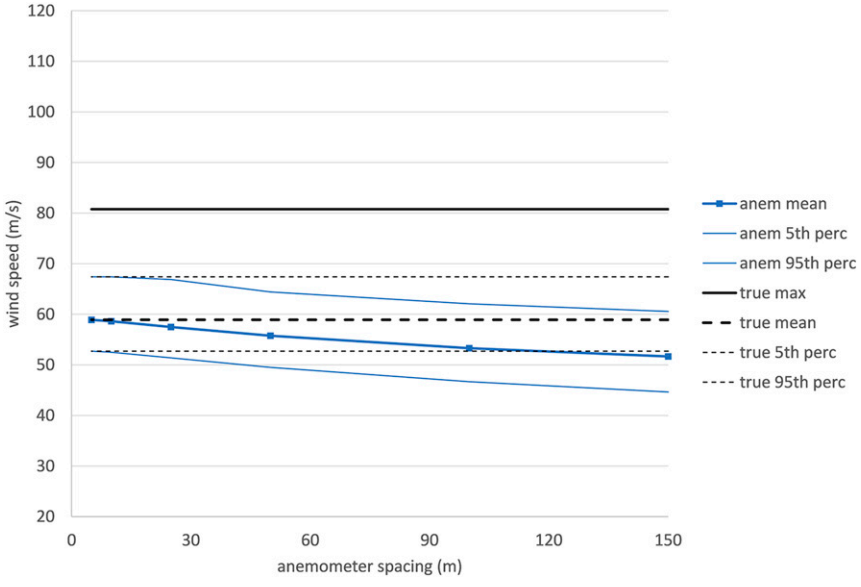

FIG. 16. As in Fig. 11, but for simulation W40SR02U10.

to observe EF5 damage approaches 40% in this case due to spatial undersampling and weak, nonresidential structures comprising a large proportion of the DIs.

We also evaluate the reliability of in situ vortex core wind speed measurements sought in previous field studies by repeatedly placing columns of perfect anemometers perpendicular to the wind swaths. The results suggest that obtaining a measurement within $5\,m\,s^{-1}$ of the true maximum wind speed at the time of observation (on average) would require three or more simultaneous measurements with the vortex, which in turn would require an anemometer spacing of 100 m or less for an average-sized tornado. Moreover, the correlation between observed and true maxima for the column in which the anemometers are located begins to drop off sharply for spacing >25 m. These findings emphasize the incompleteness of the current in situ observational record for tornadoes.

Several caveats must be included in evaluating these results. For example, even when using the "eddy injection" technique described in BDNR, the elevation used in this study (10 m AGL) is within, although near the top of, the layer in which parameterized turbulence plays a substantial role. Moreover, power spectra computed from local S10–3s time series generally begin to drop off sharply at frequencies >1 Hz, although the spectra appear reasonable at the frequency (0.33 Hz) corresponding to the gusts used for these experiments. (We also note in hindsight that low-swirl simulation W40SR005U10 is an outlier in most of the tests, suggesting that even the vortex core may not be well resolved in that case.) These facts suggest the possibility that aspects of the natural variability of tornadic winds that cannot be reproduced in these simulations may not be negligible.

Furthermore, although these results are not very sensitive to path length since the simulated vortices are near a statistical steady state, violent tornadoes in reality tend to have much longer path lengths (Brooks 2004) with much greater variability in size and intensity. In particular, if the wind swaths in Fig. 2 are taken to represent the "mature" (near peak intensity, near steady state) portions of tornado tracks, one would expect that sampling the full paths (including the "developing" and "decaying" phases) in the same manner would produce greater mean underestimates of the global maximum S10–3s than those shown here. Based on these facts, we conclude that the expected errors indicated by these experiments should be regarded as lower-bound estimates.

We have also confined this work to rural and semirural areas, leaving the question open as to what a similar analysis of DIs in an urban or suburban area would produce. However, such an analysis faces additional complications. For example, placing a large number of structures in the tornado's path would be expected to alter tornado intensity and morphology through factors such as increased broadscale surface roughness (see NDBR), localized interference from more robust surface elements (Lewellen 2014), and debris loading (Gong 2006; Lewellen et al. 2008; Bodine et al. 2016). Not only are these factors difficult and expensive to model realistically in terms of their effects on the tornado, but they are also expected to have nontrivial secondary effects on the damage produced (e.g., with debris strikes compounding the dynamic effect of the winds on structures).

Finally, as acknowledged in the introduction, our assumption that the degrees of damage specified in the enhanced Fujita scale provide a perfect indication of the maximum S10–3s impacting a structure is clearly incorrect. Even laying aside subjective variability in assigning damage ratings (Edwards 2003), this problem is highlighted by instances of adjacent structures receiving widely disparate EF ratings despite presumably being impacted by similar winds (e.g., Marshall et al. 2008, 2014). However, the bias introduced by these uncertainties is unclear; for instance, while the effects of poor construction, debris strikes, and more protracted gusts contribute to *overestimation* of maximum S10–3s, it is also apparent that chronic undersampling (particularly in sparsely populated areas) and structural limitations of DIs contribute to *underestimation*. We see observational experiments of this sort as a natural step toward quantifying the relative impacts of such error sources as part of the larger effort to improve tornado risk analysis.

Acknowledgments. This work was supported in part by the National Science Foundation through Grant AGS-1265899. We acknowledge high performance computing support from Yellowstone (ark:/85065/d7wd3xhc) provided by the Computational and Informational Systems Laboratory at the National Center for Atmospheric Research, also sponsored by the National Science Foundation. The authors also wish to thank Timothy Marshall, Gabriel Garfield, John Schroeder, and James Marquis for providing damage survey data and collaboration.

REFERENCES

Agee, E. M., 1970: Purdue tornado project activities—Part II. *Bull. Amer. Meteor. Soc.*, **51**, 951.

Alexander, C. W., and J. Wurman, 2008: Updated mobile radar climatology of supercell tornado structures and dynamics. *24th Conf. on Severe Local Storms,* Savannah, GA, Amer. Meteor. Soc., 19.4. [Available online at http://ams.confex.com/ams/pdfpapers/141821.pdf.]

Baerenzung, J., D. Rosenberg, P. D. Mininni, and A. Pouquet, 2011: Helical turbulence prevails over inertial waves in forced rotating flows at high Reynolds and low Rossby numbers. *J. Atmos. Sci.*, **68**, 2757–2770, doi:10.1175/2010JAS3445.1.

Bedard, A. J., Jr., and C. Ramzy, 1983: Surface meteorological observations in severe thunderstorms. Part I: Design details of TOTO. *J. Climate Appl. Meteor.*, **22**, 911–918, doi:10.1175/1520-0450(1983)022<0911:SMOIST>2.0.CO;2.

Blair, S. F., D. R. Deroche, and A. E. Pietrycha, 2008: In situ observations of the 21 April 2007 Tulia, Texas tornado. *Electron. J. Severe Storms Meteor.*, **3** (3). [Available online at http://www.ejssm.org/ojs/index.php/ejssm/article/view/39.]

Blanchard, D. O., 2013: A comparison of wind speed and forest damage associated with tornadoes in northern Arizona. *Wea. Forecasting*, **28**, 408–417, doi:10.1175/WAF-D-12-00046.1.

Bluestein, H. B., 1983: Surface meteorological observations in severe thunderstorms. Part II: Field experiments with TOTO. *J. Climate Appl. Meteor.*, **22**, 919–930, doi:10.1175/1520-0450(1983)022<0919:SMOIST>2.0.CO;2.

Bodine, D. J., T. Maruyama, R. D. Palmer, C. J. Fulton, H. B. Bluestein, and D. C. Lewellen, 2016: Sensitivity of tornado dynamics to soil debris loading. *J. Atmos. Sci.*, **73**, 2783–2801, doi:10.1175/JAS-D-15-0188.1.

Brock, F. V., G. Lesins, and R. Walko, 1987: Measurement of pressure and air temperature near severe thunderstorms: An inexpensive and portable instrument. *Extended Abstracts, Sixth Symp. on Meteorological Observations and Instrumentation,* New Orleans, LA, Amer. Meteor. Soc., 320–323.

Brooks, H. E., 2004: On the relationship of tornado path length and width to intensity. *Wea. Forecasting*, **19**, 310–319, doi:10.1175/1520-0434(2004)019<0310:OTROTP>2.0.CO;2.

Bryan, G. H., and J. M. Fritsch, 2002: A benchmark simulation for moist nonhydrostatic numerical models. *Mon. Wea. Rev.*, **130**, 2917–2928, doi:10.1175/1520-0493(2002)130<2917:ABSFMN>2.0.CO;2.

——, N. A. Dahl, D. S. Nolan, and R. Rotunno, 2017a: An eddy injection method for large-eddy simulations of tornado-like vortices. *Mon. Wea. Rev.*, **145**, 1937–1961, doi:10.1175/MWR-D-16-0339.1.

——, R. P. Worsnop, J. K. Lundquist, and J. A. Zhang, 2017b: A simple method for simulating wind profiles in the boundary layer of tropical cyclones. *Bound.-Layer Meteor.*, **162**, 475–502, doi:10.1007/s10546-016-0207-0.

Burgess, D. B., M. A. Magsig, J. Wurman, D. C. Dowell, and Y. Richardson, 2002: Radar observations of the 3 May 1999 Oklahoma City tornado. *Wea. Forecasting*, **17**, 456–471, doi:10.1175/1520-0434(2002)017<0456:ROOTMO>2.0.CO;2.

Colgate, S., 1982: Small rocket tornado probe. Preprints, *12th Conf. on Severe Local Storms*, San Antonio, TX, Amer. Meteor. Soc., 396–400.

Doswell, C. A., III, and D. W. Burgess, 1988: Some issues of United States tornado climatology. *Mon. Wea. Rev.*, **116**, 495–501, doi:10.1175/1520-0493(1988)116<0495:OSIOUS>2.0.CO;2.

——, H. E. Brooks, and N. Dotzek, 2009: On the implementation of the enhanced Fujita scale in the USA. *Atmos. Res.*, **93**, 554–563, doi:10.1016/j.atmosres.2008.11.003.

Dowell, D. C., C. R. Alexander, J. M. Wurman, and L. J. Wicker, 2005: Centrifuging of hydrometeors and debris in tornadoes: Radar reflectivity patterns and wind measurement errors. *Mon. Wea. Rev.*, **133**, 1501–1524, doi:10.1175/MWR2934.1.

Edwards, R., 2003: Rating tornado damage: An exercise in subjectivity. Preprints, *Symp. on the F-Scale and Severe-Weather Damage Assessment*, Long Beach, CA, Amer. Meteor. Soc., P1.2. [Available online at http://ams.confex.com/ams/pdfpapers/55307.pdf.]

——, J. G. LaDue, J. T. Ferree, K. Scharfenberg, C. Maier, and W. L. Coulbourne, 2013: Tornado intensity estimation: Past, present, and future. *Bull. Amer. Meteor. Soc.*, **94**, 641–653, doi:10.1175/BAMS-D-11-00006.1.

Fiedler, B. H., 1994: The thermodynamic speed limit and its violation in axisymmetric numerical simulations of tornado-like vortices. *Atmos.–Ocean*, **32**, 335–359, doi:10.1080/07055900.1994.9649501.

——, and G. S. Garfield, 2010: Axisymmetric tornado simulations with various turbulence models. *Comput. Fluid Dyn. Lett.*, **2**, 112–121.

Fujita, T. T., 1970: The Lubbock tornadoes: A study of suction spots. *Weatherwise*, **23**, 161–173, doi:10.1080/00431672.1970.9932888.

——, 1971: Proposed characterization of tornadoes and hurricanes by area and intensity. SMRP Research Paper 91, University of Chicago, Chicago, IL, 42 pp. [Available from Wind Engineering Research Center, Box 41023, Lubbock, TX 79409.]

Gong, B., 2006: Large-eddy simulation of the effects of debris on tornado dynamics. Ph.D. thesis, West Virginia University, 187 pp.

Houser, J. B., H. B. Bluestein, and J. C. Snyder, 2015: Rapid-scan, polarimetric, Doppler radar observations of tornadogenesis and tornado dissipation in a tornadic supercell: The ''El Reno, Oklahoma'' storm of 24 May 2011. *Mon. Wea. Rev.*, **143**, 2685–2710, doi:10.1175/MWR-D-14-00253.1.

Karstens, C. D., T. M. Samaras, B. D. Lee, W. A. Gallus Jr., and C. A. Finley, 2010: Near-ground pressure and wind measurements in tornadoes. *Mon. Wea. Rev.*, **138**, 2570–2588, doi:10.1175/2010MWR3201.1.

Kato, R., and Coauthors, 2015: Analysis of the horizontal two-dimensional near-surface structure of a winter tornadic vortex using high-resolution in situ wind and pressure measurements. *J. Geophys. Res. Atmos.*, **120**, 5879–5894, doi:10.1002/2014JD022878.

Kolmogorov, A. N., 1941: The local structure of turbulence in incompressible viscous fluid for very large Reynolds numbers. *Dokl. Akad. Nauk SSSR*, **30**, 299–303.

Kosiba, K. A., and J. Wurman, 2013: The three-dimensional structure and evolution of a tornado boundary layer. *Wea. Forecasting*, **28**, 1552–1561, doi:10.1175/WAF-D-13-00070.1.

——, ——, Y. Richardson, P. Markowski, and P. Robinson, 2013: Genesis of the Goshen County, Wyoming, tornado on 5 June 2009 during VORTEX2. *Mon. Wea. Rev.*, **141**, 1157–1181, doi:10.1175/MWR-D-12-00056.1.

Lee, B. D., C. A. Finley, and T. M. Samaras, 2011: Surface analysis near and within the Tipton, Kansas, tornado on 29 May 2008. *Mon. Wea. Rev.*, **139**, 370–386, doi:10.1175/2010MWR3454.1.

Lee, J. J., T. M. Samaras, and C. R. Young, 2004: Pressure measurements at the ground in an F-4 tornado. *22nd Conf. on Severe Local Storms*, Hyannis, MA, Amer. Meteor. Soc., 15.3. [Available online at https://ams.confex.com/ams/11aram22sls/techprogram/paper_81700.htm.]

Lewellen, D. C., 2014: Local roughness effects on tornado dynamics. *27th Conf. on Severe Local Storms*, Madison, WI, Amer. Meteor. Soc., 15A.1. [Available online at https://ams.confex.com/ams/27SLS/webprogram/Paper254357.html.]

——, W. S. Lewellen, and J. Xia, 2000: The influence of a local swirl ratio on tornado intensification near the surface. *J. Atmos. Sci.*, **57**, 527–544, doi:10.1175/1520-0469(2000)057<0527:TIOALS>2.0.CO;2.

——, B. Gong, and W. S. Lewellen, 2008: Effects of finescale debris on near-surface tornado dynamics. *J. Atmos. Sci.*, **65**, 3247–3262, doi:10.1175/2008JAS2686.1.

Marshall, T. P., 2002: Tornado damage survey at Moore, Oklahoma. *Wea. Forecasting*, **17**, 582–598, doi:10.1175/1520-0434(2002)017<0582:TDSAMO>2.0.CO;2.

——, D. W. McCarthy, J. G. LaDue, J. Wurman, C. Alexander, P. Robinson, and K. Kosiba, 2008: Damage survey of the Greensburg, KS tornado. *24th Conf. on Severe Local Storms*, Savannah, GA, Amer. Meteor. Soc., 8B.3. [Available online at http://ams.confex.com/ams/pdfpapers/141534.pdf.]

——, D. Burgess, G. Garfield, J. Snyder, R. Smith, D. Speheger, and H. Bluestein, 2014: Ground-based damage survey and radar analysis of the El Reno, Oklahoma tornado. *27th Conf. on Severe Local Storms*, Madison, WI, Amer. Meteor. Soc., 13.1. [Available online at https://ams.confex.com/ams/27SLS/webprogram/Paper254342.html.]

Mininni, P. D., and A. Pouquet, 2010: Rotating helical turbulence. I. Global evolution and spectral behavior. *Phys. Fluids*, **22**, 035105, doi:10.1063/1.3358466.

Nolan, D. S., 2005: A new scaling for tornado-like vortices. *J. Atmos. Sci.*, **62**, 2639–2645, doi:10.1175/JAS3461.1.

——, J. A. Zhang, and D. P. Stern, 2009a: Evaluation of planetary boundary layer parameterizations in tropical cyclones by comparison of in situ observations and high-resolution simulations of Hurricane Isabel (2003). Part I: Initialization, maximum winds, and the outer-core boundary layer. *Mon. Wea. Rev.*, **137**, 3651–3674, doi:10.1175/2009MWR2785.1.

——, ——, and ——, 2009b: Evaluation of planetary boundary layer parameterizations in tropical cyclones by comparison of in situ observations and high-resolution simulations of Hurricane Isabel (2003). Part II: Inner-core boundary layer and eyewall structure. *Mon. Wea. Rev.*, **137**, 3675–3698, doi:10.1175/2009MWR2786.1.

——, R. Atlas, K. T. Bhatia, and L. R. Bucci, 2013: Development and validation of a hurricane nature run using the joint OSSE nature run and the WRF model. *J. Adv. Model. Earth Syst.*, **5**, 382–405, doi:10.1002/jame.20031.

——, J. A. Zhang, and E. W. Uhlhorn, 2014: On the limits of estimating the maximum wind speeds in hurricanes. *Mon. Wea. Rev.*, **142**, 2814–2837, doi:10.1175/MWR-D-13-00337.1.

——, N. A. Dahl, G. H. Bryan, and R. Rotunno, 2017: Tornado vortex structure, intensity, and surface wind gusts in large-eddy simulations with fully developed turbulence. *J. Atmos. Sci.*, **74**, 1573–1597, doi:10.1175/JAS-D-16-0258.1.

Phan, L., and E. Simiu, 1998: The Fujita tornado intensity scale: A critique based on observations of the Jarrell tornado of May 27, 1997. NIST Tech. Note 1426, 20 pp. [NTIS PB98-175136INZ.]

Rasmussen, E. N., J. M. Straka, R. Davies-Jones, C. A. Doswell III, F. H. Carr, M. D. Eilts, and D. R. MacGorman, 1994: Verification of the origins of rotation in tornadoes experiment: VORTEX. *Bull. Amer. Meteor. Soc.*, **75**, 995–1006, doi:10.1175/1520-0477(1994)075<0995:VOTOOR>2.0.CO;2.

Reynolds, G. W., 1971: Complication in estimating the magnitudes of tornado forces from damage analysis. Preprints, *Seventh Conf. on Severe Local Storms,* Kansas City, MO, Amer. Meteor. Soc., 179–182.

Rotunno, R., 2013: The fluid dynamics of tornadoes. *Annu. Rev. Fluid Mech.*, **45**, 59–84, doi:10.1146/annurev-fluid-011212-140639.

——, G. H. Bryan, D. S. Nolan, and N. A. Dahl, 2016: Axisymmetric tornado simulations at high Reynolds number. *J. Atmos. Sci.*, **73**, 3843–3854, doi:10.1175/JAS-D-16-0038.1. 1.

Samaras, T. M., and J. J. Lee, 2004: Pressure measurements within a large tornado. *Eighth Symp. on Integrated Observing and Assimilation Systems for Atmosphere, Oceans, and Land Surface*, Seattle, WA, Amer.Meteor. Soc., 4.9. [Available online at http://ams.confex.com/ams/84Annual/techprogram/paper_74267.htm.]

Schaefer, J. T., and J. G. Galway, 1982: Population biases in the tornado climatology. Preprints, *12th Conf. on Severe Local Storms*, San Antonio, TX, Amer. Meteor. Soc., 51–54.

Snyder, J. C., and H. B. Bluestein, 2014: Some considerations for the use of high-resolution mobile radar data in tornado intensity determination. *Wea. Forecasting*, **29**, 799–827, doi:10.1175/WAF-D-14-00026.1.

Taylor, G. I., 1938: The spectrum of turbulence. *Proc. Roy. Soc. London*, **132A**, 476–490.

Uhlhorn, E. W., and D. S. Nolan, 2012: Observational undersampling in tropical cyclones and implications for estimated intensity. *Mon. Wea. Rev.*, **140**, 825–840, doi:10.1175/MWR-D-11-00073.1.

Wakimoto, R. M., N. T. Atkins, K. M. Butler, H. B. Bluestein, K. Thiem, J. Snyder, and J. Houser, 2015: Photogrammetric analysis of the 2013 El Reno tornado combined with mobile X-band polarimetric radar data. *Mon. Wea. Rev.*, **143**, 2657–2683, doi:10.1175/MWR-D-15-0034.1.

Wicker, L. J., and W. C. Skamarock, 2002: Time splitting methods for elastic models using forward time schemes. *Mon. Wea. Rev.*, **130**, 2088–2097, doi:10.1175/1520-0493(2002)130<2088:TSMFEM>2.0.CO;2.

Wind Science and Engineering Center, 2006: A recommendation for an enhanced Fujita scale. Texas Tech University, National Wind Institute, 111 pp. [Available online at http://www.depts.ttu.edu/nwi/Pubs/EnhancedFujitaScale/EFScale.pdf.]

Winn, W. P., S. J. Hunyady, and G. D. Aulich, 1999: Pressure at the ground in a large tornado. *J. Geophys. Res.*, **104**, 22 067–22 082, doi:10.1029/1999JD900387.

Wurman, J., and S. Gill, 2000: Finescale radar observations of the Dimmitt, Texas (2 June 1995), tornado. *Mon. Wea. Rev.*, **128**, 2135–2164, doi:10.1175/1520-0493(2000)128<2135:FROOTD>2.0.CO;2.

——, and T. Samaras, 2004: Comparison of in-situ pressure and DOW Doppler winds in a tornado and RHI vertical slices through 4 tornadoes during 1996-2004. *22nd Conf. on Severe Local Storms*, Hyannis, MA, Amer. Meteor. Soc., 15.4. [Available online at http://ams.confex.com/ams/11aram22sls/techprogram/paper_82352.htm.]

——, C. Alexander, P. Robinson, and Y. Richardson, 2007: Low-level winds in tornadoes and potential catastrophic tornado impacts in urban areas. *Bull. Amer. Meteor. Soc.*, **88**, 31–46, doi:10.1175/BAMS-88-1-31.

——, D. Dowell, Y. Richardson, P. Markowski, E. Rasmussen, D. Burgess, L. Wicker, and H. B. Bluestein, 2012: The Second Verification of the Origins of Rotation in Tornadoes Experiment: VORTEX2. *Bull. Amer. Meteor. Soc.*, **93**, 1147–1170, doi:10.1175/BAMS-D-11-00010.1.

——, K. Kosiba, and P. Robinson, 2013: In situ, Doppler radar, and video observations of the interior structure of a tornado and the wind–damage relationship. *Bull. Amer. Meteor. Soc.*, **94**, 835–846, doi:10.1175/BAMS-D-12-00114.1.

——, ——, ——, and T. Marshall, 2014: The role of multiple vortex tornado structure in causing storm researcher fatalities. *Bull. Amer. Meteor. Soc.*, **95**, 31–45, doi:10.1175/BAMS-D-13-00221.1.